Performance Investigation of Zinc Propellant in sub kW class Hall Thrusters

IEPC-2022-284

V.G. Tirila[1] and C. Ryan[2]
Faculty of Engineering and the Environment, University of Southampton, United Kingdom

A. Demairé[3] and A. Hallock[4]
OHB Sweden, Viderögatan 6, 164 40 Kista, SE-164, Sweden

    Zinc was successfully integrated and tested in sub-kW class Hall thrusters as an alternative propellant to xenon. The advantages of zinc include a high storage density, low first ionization energy, potentially high specific impulse and low cost. The third iteration (Mark 3) of a novel propellant storage and delivery system (PSDS) for solid propellants was tested and experimentally characterised, demonstrating operational zinc outputs up to 0.36 mg/s in sublimation mode with a peak of 8.2 mg/s near the melting point of zinc. The PSDS power consumption was approximately 20-30 W during thruster operation and 50 W in the start-up sequence. A 100 W laboratory cylindrical Hall thruster (CHT-100) was modified structurally and magnetically to couple with the PSDS Mark 3. Performance was measured during thruster operation on xenon, krypton and zinc with a mass flow rate of 5 SCCM to 10 SCCM, a discharge power of 50-150 W and an electromagnet current of 0.8 A on the main solenoid and 1.0 A on the secondary solenoid. Measured thrust was 1 mN during operation on zinc at an input power of 80 W and 1.2 mN during operation on krypton at an input power of 98 W. At an input power of 80 W the maximum measured specific impulse was 448 s during operation on zinc and 371 s during operation on krypton. Demonstration of throttling and PSDS redundancy in failure mode operation is discussed, as well as deposition and channel erosion.

I. Nomenclature

$\dot{m}_p$	=	propellant mass flow rate	Re	=	Reynolds number
P_v	=	vapor pressure	σ	=	collision diameter of the element
P_c	=	vacuum chamber pressure	ϵ/k	=	Lennard-Jones depth of potential-energy minimum
ρ_v	=	vapor density	ΔT_{c-s}	=	core to surface temperature difference
T	=	slug surface temperature	α	=	thrust balance calibration factor
M	=	molecular mass	δ_d	=	displacement measured on thruster shutdown
D	=	hydraulic diameter	F	=	thrust
L	=	hollow anode slot length	P_a	=	anode power
f_D	=	Darcy friction factor	I_{sp}	=	specific impulse
μ	=	propellant viscosity	η_a	=	anode efficiency

.

[1]PhD Student, Astronautics Group, University of Southampton, v-g.tirila@soton.ac.uk
[2]Lecturer, Astronautics Group, University of Southampton, c.n.ryan@soton.ac.uk
[3]OHB Sweden Propulsion BD, OHB Sweden AB, alain.demaire@ohb-sweden.se
[4]Electric Propulsion Specialist, OHB Sweden AB, ashley.hallock@ohb-sweden.se

II. Introduction

T<small>HIS</small> paper describes the progress made in an ongoing three-year project supported by the University of Southampton and OHB Sweden. The goal of the project is to design, develop and test an EP system consisting of a propellant storage and delivery system (PSDS) and a Hall thruster that can be used with a variety of solid propellants. This paper presents the final development stage of the PSDS, experimental results for PSDS output with zinc, and the initial performance results of zinc as an alternative propellant in a 100 W cylindrical Hall thruster, concluding the second phase of the three-year project.

A. Motivation

The increasing number of launches and the diversification of mission scenarios to include smaller, more accessible orbital platforms coupled with increased use and popularity of electric propulsion (EP) systems [1] has motivated development towards more sustainable propellants [2]. Traditional EP systems first successfully used xenon as a propellant shortly after their first few orbital demonstrations in satellites 50 years ago. Ever since, xenon has been the de-facto choice due to its non-toxicity, non-reactivity, high atomic mass (131.293 u) and good ionization properties (12.1 eV first ionization potential and 5.0e-16 cm^2 peak ionization cross-section) [3]. Yet xenon is a rare gas with production limited by its concentration in air and the subsequent low yield resulting from the process of separation of air into oxygen and nitrogen [4]. Due to its extensive use in other major industries for example as an anaesthetic agent or part of automotive lighting systems, xenon availability and price are in constant fluctuation [5] which can strain the project budget and schedule as the cost of propellant may become a significant fraction of the project expenditure.

Considerable efforts have been made towards investigating viable alternatives to xenon [6] [7][8] [2] [9] [10] [11] [12] [13] [14] [15]. The most notable and widely used is krypton [12] [16] with a lighter atomic mass (83.798 u) and less favorable ionization properties (14 eV first ionization potential and 3.7e-16 cm^2 peak ionization cross-section) [3]. Consequently it can replicate the performance of xenon albeit at a lower efficiency [16]. The volume penalty for krypton is higher with a density one third that of xenon under storage pressure whilst the cost associated is still significant since krypton is a rare gas produced together with xenon [4]. Nonetheless, krypton is widely used in ground testing and in orbit most notably in the Starlink constellation. Gases such as argon [14], nitrogen [13], and oxygen [15] amongst others are further proposed as potential propellants in larger EP thrusters and are an active area of research.

B. Condensable Propellants

Condensable propellants, which are propellants found in either solid or liquid form at normal temperature and pressure, have been proposed as a possible alternative to xenon. The major advantage of this class of propellants is the high density of the elements that allow significant volume savings over pressurised gasses such as xenon (up to 6 times higher volume) or krypton (up to 19 times higher volume). To produce a gaseous flow necessary for thruster operation, condensable propellants require heating at low ambient pressure above an element-specific temperature threshold. The gas phase forms as a saturated vapor with a temperature-dependent pressure either through the process of sublimation or evaporation.

Currently, the leading research in alternative EP propellants is focused on iodine [2] which has a similar atomic mass to xenon at 126.904 u and theoretically better ionization properties 10.5 eV first ionization potential and 6.0e-16 cm^2 peak ionization cross-section). Iodine sublimates at low temperature and achieves a high vapor pressure (23 kPa below $113.7°C$) at low input power compared to the total thruster input power, making it a desirable propellant. Experimentally measured Hall thruster performance is comparable for operation on iodine and xenon [7]. However, iodine is not a perfect xenon alternative due to its corrosive nature [17] that makes ground testing difficult and may impact the lifetime of the thruster. Other potential condensable propellants, such as zinc, magnesium and bismuth, offer a unique set of advantages and disadvantages. Operation on bismuth (208.980 u) was shown to provide higher thrust to power ratios compared to xenon [6] while magnesium (24.305 u) and zinc (65.38 u) may potentially provide higher specific impulse and efficiency [9]. Unlike bismuth which has a naturally low scaling vapor pressure requiring temperatures higher than 700-800 $°C$ for pressures greater than 10 Pa [6], zinc and magnesium can achieve comparable gas phase pressure at lower temperatures in the 380-550 $°$ C temperature range [18].

Investigations of operation on zinc and magnesium of kW-class Hall thrusters optimised for xenon can be found in [9] [11] [10]. It is the aim of this projects to investigate the use of zinc and magnesium in sub-kW class Hall thrusters and to provide a clear understanding of the behaviour of metallic condensable propellants during thruster operation. This paper details the development and performance review of a novel propellant storage and delivery system (PSDS) for metallic, condensable propellants. The modification of an existing 100 W cylindrical Hall thruster is detailed and the

PSDS - thruster coupling discussed. Operational performance data from the cylindrical Hall thruster on zinc, xenon and krypton is reviewed and the findings are assessed.

III. Propellant Storage and Delivery System (PSDS)

Unlike gaseous propellants which can be used directly from a pressurised state, metallic propellants have element-specific temperature requirements for conversion to the gaseous phase. Zinc sublimates at temperatures of approximately $300\,^{\circ}C$ to $420\,^{\circ}C$ while magnesium sublimates at temperatures of approximately $400\,^{\circ}C$ to $650\,^{\circ}C$ in a low pressure environment (<0.01 Pa). The end of the sublimation interval is represented by the melting point of the element. Higher gas phase pressures are achievable through evaporation from liquid metals at temperatures higher than the melting point at the cost of extra power required for latent heat during phase changes and for heating the propellant to higher temperatures. A metallic propellant storage and delivery system makes use of the two principles, sublimation and evaporation, to sustain a gas phase pressure sufficient for propellant transport to the discharge chamber of the thruster.

The delivery of metallic propellants to the thruster has been investigated and can be achieved in various different manners. An externally heated reservoir of molten metal can be utilised with a heated feed line to deliver the evaporated gas to the discharge chamber [9]. Alternatively the anode can be machined from the propellant material and the sublimation rate controlled via a secondary shim anode that balances the discharge, restricting the heating of the primary anode [11]. Finally, a porous anode may become the vaporizer by heating liquid propellant pumped from an external tank [10]. Spool-fed metal wires have also been used in combination with a vaporizer to supply a flow of metallic propellant [9].

A. Mark 3 Iteration

The Mark 3 PSDS developed in this project adopts a unique design shown in Fig 1 and 2, additively manufactured in 316 stainless steel. In this design the propellant is sublimated externally and distributed through a novel hollow anode that functions as a feed line. The solid propellant slug (15 mm diameter, 22.5 mm length) is heated by a 6.35 mm diameter cartridge heater with a built-in thermocouple. Upon heating the cartridge heater and the annular propellant slug, the components expand into each other forming a good conductive connection and improving the accuracy of temperature measurements. Two additional 6.35 mm diameter cartridge heaters with built-in thermocouples control the temperature of the tank. The influx of gas from the propellant storage volume is directed via two oval slots to the discharge chamber. At start-up, the colder hollow anode leads to the condensation of a portion of propellant in the vicinity of the walls. However, a sufficient flow rate to the discharge chamber is still established due to the large cross-sectional area. At ignition the hollow anode heats up and effectively purges the condensed propellant from the
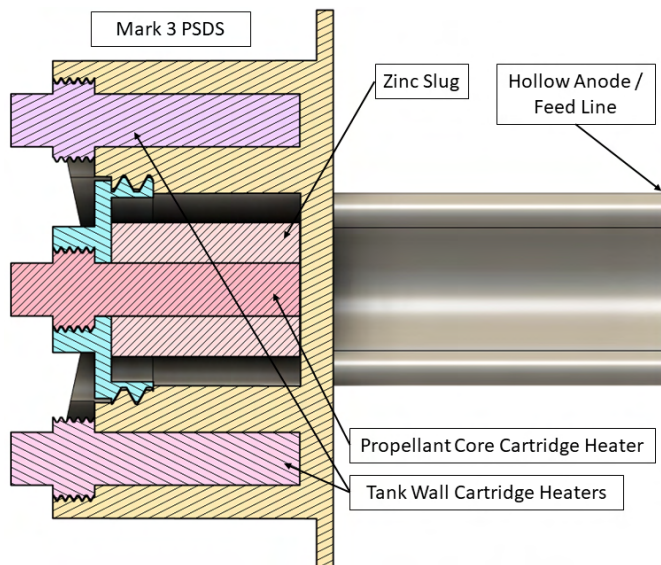

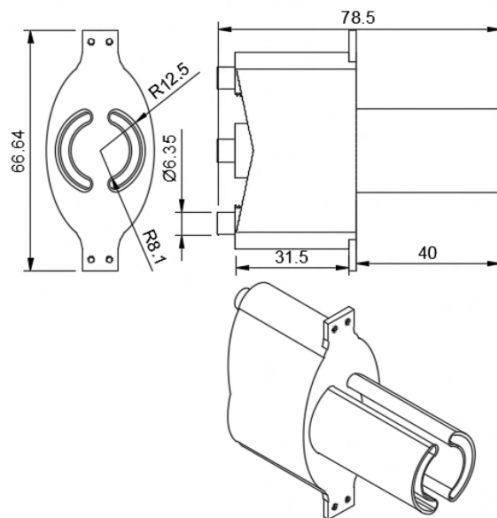Fig. 1   Mark 3 PSDS - section view - CAD.

Fig. 2   Mark 3 PSDS - key dimensions in mm.

walls. The residual heat from the discharge is conducted through the hollow anode to the tank, reducing the heater power input. The advantages of this design are precise propellant output, minimal power utilization, scalability, and propellant versatility as any solid element that can achieve a vapor pressure > 10 Pa at temperatures below the melting point can be utilized.

B. Flow Model

The most important and difficult aspect of metallic propellant usage and integration is flow control. Unlike gaseous propellant, the pressure of metallic propellant is not registered by conventional pressure sensors and the temperatures required to prevent condensation and ensure a stable gaseous phase exceeds the design temperature of most flow controllers. Thus indirect estimations are used to calculate the propellant output. Previous investigations derive the flow rate through discharge current measurements and known thruster efficiencies [9]. Mechanical wire feed rate may be used [9], electromagnetic pumping rates in the case of liquid metal propellants [19], or the direct sublimation rate equation when the propellant is contained within the anode [11]. Otherwise, mass measurement subtraction before and after the test provides a good estimation of the propellant flow rate if a constant temperature is maintained throughout the experiment.

In this case, the Mark 3 PSDS flow model is constructed using the temperature profile of the propellant core in conjunction with mass measurements before and after the test. The flow rate model was based on the Darcy–Weisbach equation due to the experimentally determined high dependency on cross-sectional area. [18].

$$\dot{m}_p = \pi \sqrt{\frac{\rho_v (P_v - P_c) D^5}{8 L f_D}} \tag{1}$$

The viscosity of the propellant is then estimated [20] to obtain an indication of the Reynolds number range in which the propellant is more likely to be at during PSDS operation.

$$\mu = \frac{16.64 T \sqrt{M}}{\sigma^2 \sqrt{\epsilon/k}} \tag{2}$$

In gas phase, zinc is shown to be more viscous (3.57e-5 Pa s) than other propellants such as xenon (2.12e-5 Pa s), magnesium (1.63e-5 Pa s) or iodine (1.14e-5 Pa s) at normal operating temperatures. The pressure difference is then calculated between the vacuum chamber pressure, P_c and the vapor pressure of the propellant element, P_v. The vapor pressure at a specific propellant slug surface temperature is calculated from the following equation.

$$log(P_v) = 5.006 + A + B + T^{-1} + C \, log(T) + D T^{-3} \tag{3}$$

Where A, B, C and D are empirical coefficients specific to the element in solid form [21]. Increased viscosity coupled with a low maximum pressure differential from sublimation (approximately 21 Pa at 420 $°C$) indicate a potential laminar flow regime for zinc gas. A laminar form for the Darcy friction factor [22] matched the range of experimental results and was selected for the estimation model. Zinc deposition patterns inside the hollow anode further suggest the existence of a relatively slow velocity front.

$$f_D = \frac{64}{Re} \tag{4}$$

The Reynolds number can be calculated as a function of the propellant flow rate, viscosity and PSDS geometry according to the following equation.

$$Re = \frac{4 \dot{m}_p}{\pi D \mu} \tag{5}$$

Using this set of equations, the flow rate may be calculated for the Mark 3 geometry. The resulting flow rate for zinc is shown in Fig 3 and for magnesium in Fig 4 given a surface propellant temperature. This represents a hard theoretical limit imposed by the cross-sectional area of the PSDS in the form of the hydraulic diameter D. The PSDS hollow anode area is subsequently limited by the size of the thruster discharge channel. With a higher-power thruster, a consequently larger discharge channel cross-sectional area accommodates a larger PSDS which has an increased hydraulic diameter from which propellant transport benefits according to Equation 1.

In practice, the propellant is heated from the core through a non-negligible propellant thickness. The heater also has a fundamentally imperfect conduction path to the propellant which is dependent on machined tolerances. As a result,
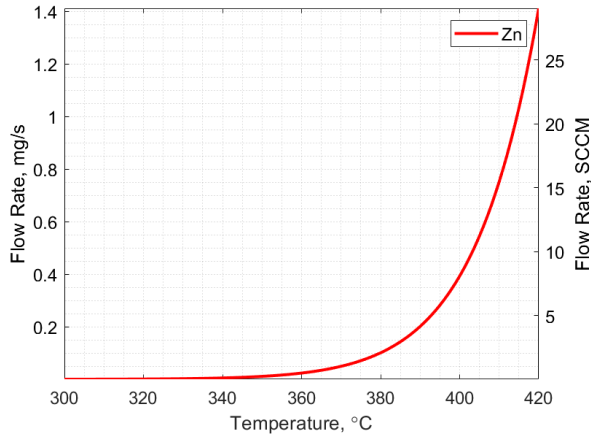
Fig. 3 Ideal zinc flow rate estimation based on slug surface temperature.
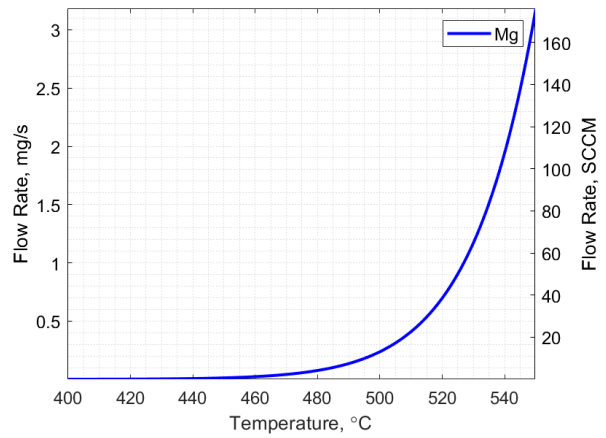

Fig. 4 Ideal magnesium flow rate estimation based on slug surface temperature.

the temperature registered by the built-in thermocouple will be higher than the surface temperature. An adjustment factor ΔT_{c-s} is added to the temperature measurement to match the propellant core reading to the actual flow rate. A consequence of this is that the propellant contact point with the heater melts at a lower propellant output rate than expected as the surface of the propellant is cooler by ΔT_{c-s} degrees. In the case of zinc, a low vapor pressure resulting from sublimation coupled with an already constrained cross-sectional area and a high ΔT_{c-s} factor can make propellant output impossible in smaller, lower-power thrusters.

During experiments, given the known propellant core temperature and adjustment factor, ΔT_{c-s}, the propellant output at each point can be integrated to match the mass measurements before and after the experiment. An example of the calculated and scaled flow rate is shown in Fig 6, which was generated from the propellant temperature profile shown in Fig 5. It can be seen that small but controllable temperature changes result in a controlled change in the flow rate.
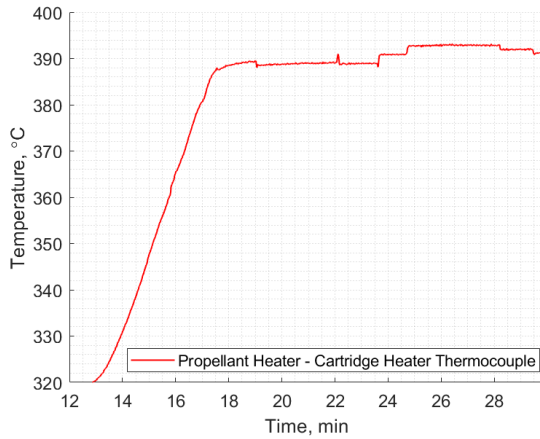
Fig. 5 Propellant temperature profile during thruster operation.
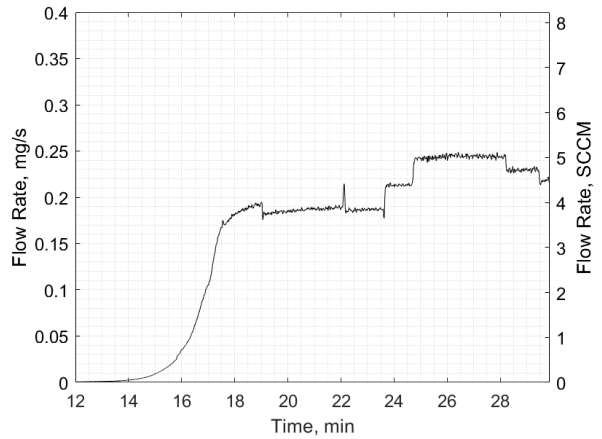
Fig. 6 Estimated propellant flow rate during thruster operation.

Experimentally, the ΔT_{c-s} factor was found to be within the range of 23 to 33 $^\circ C$ for manufactured zinc slugs and dropped to 12 $^\circ$ C in two isolated cases where melting of the slug was observed, indicating improved conduction. It is important to note that there is a time lag between temperature data acquisition and flow rate data acquisition which affects live estimations. It was observed that thruster throttling via a 2° C temperature drop takes between 30-60 seconds.

C. Thermal Design

   The Mark 3 PSDS was developed to utilize the residual heat from thruster discharge, reducing the required heater power. The propellant was found to be sufficiently thermally isolated from the propellant housing to allow fine temperature adjustments during thruster operation and propellant output throttling. In case of a heater failure, there is sufficient thermal conduction in the system to allow for a redundancy at the cost of increased power consumption from the remaining two heaters which can supplement either a propellant heater failure or a tank heater failure. The PSDS
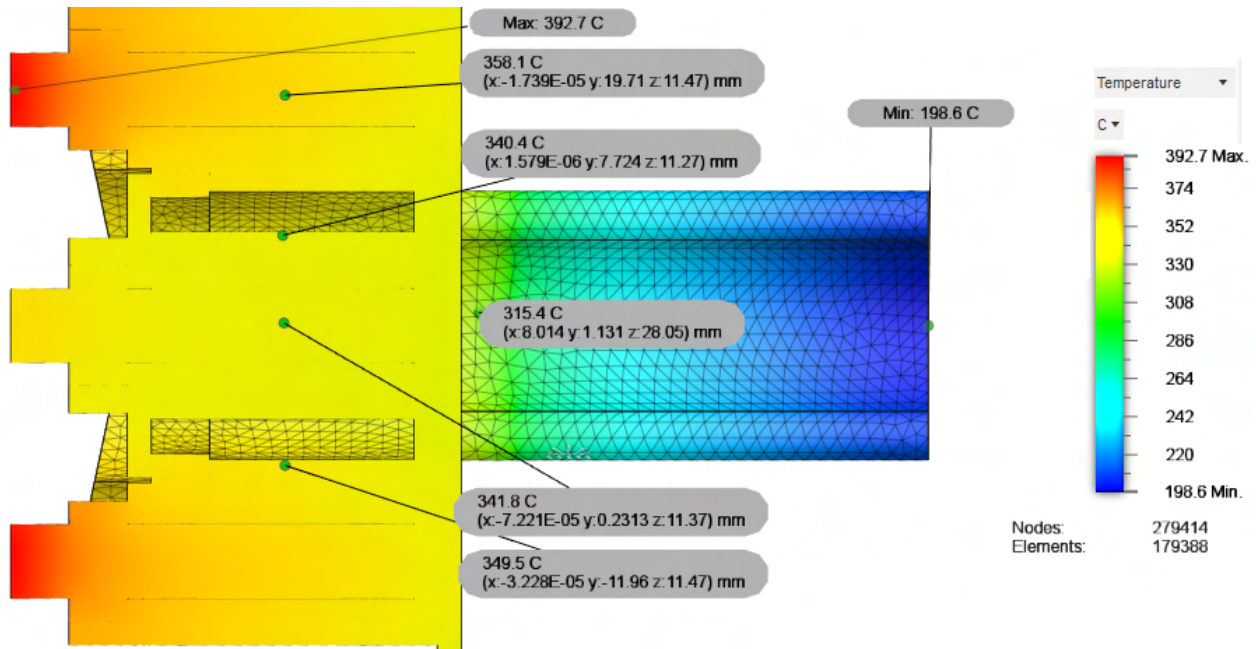
Fig. 7   Startup thermal simulation with a zinc slug - 20 W each tank wall heater - 10 W propellant core heater.
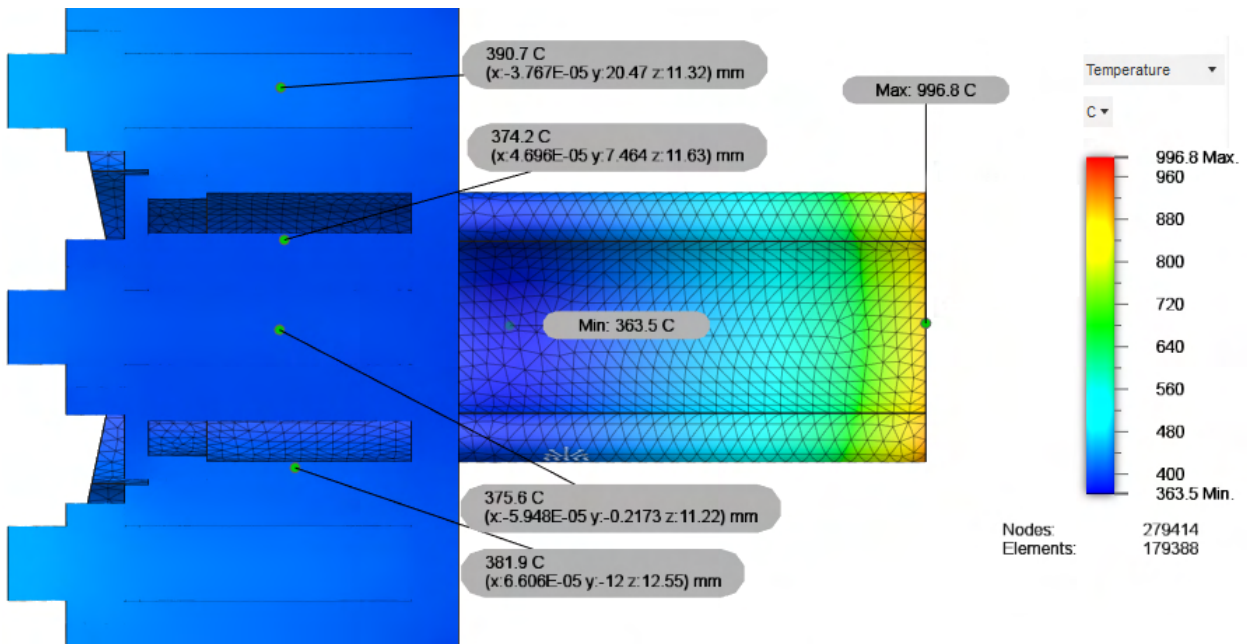
Fig. 8   Operation thermal simulation with a zinc slug - 20 W each tank wall heater - 10 W propellant core heater - 80 W anode surface heat input.

operating modes are further discussed in relation to the thruster operation in the performance data section.

Two PSDS operating conditions are simulated. In Fig 7 the initial heat-up stage is shown. The power applied to the tank wall heaters is modeled at 20 W each and the power applied to the core heater inside the zinc propellant is modelled at 10 W. No additional heating is applied to the anode. Calculations of temperatures during steady-state thruster operation are shown in Fig 8 at a residual anode heater power of 80 W, representing the conditions inside a low power thruster (CHT-100). The tank wall heater power is modeled at 20 W each and the power applied to the core heater inside the zinc propellant is modelled at 10 W. The calculated temperature is consistent across the inner wetted surfaces of the PSDS at approximately 340 $^\circ C$ for startup and 370 $^\circ C$ in operation. This suggests that the temperature feedback from the simulated discharge is manageable and still allows for independent propellant temperature control.

In experiments, in both cases, imperfect mechanical contact and a variable emissivity alter the temperature distribution. During warm-up, 50 W was found to be sufficient to reach and maintain operating conditions (>380$^\circ C$) in approximately 30 minutes. The experimental heater core - wall temperature difference was found to be 20-30 $^\circ$ C, similar to the heater core - propellant surface temperature difference. Temperatures above 600-700 $^\circ C$ were sustained at the hollow anode by a 100 W discharge during thruster operation. Upon thruster ignition, a 20 $^\circ$ C temperature increase in the walls was measured which compares well to simulation results. The Mark 3 was successfully tested up to a discharge power of 150 W without any melting or deformation in the additively manufactured 316 stainless steel structure.

D. Equipment and Methodology

Metallic propellant heater control is challenging as the propellant can conduct and cause short-circuits in the equipment. In the case of the Mark 3 PSDS, an additional challenge is retaining the isolation of the electrical circuit driving the heaters. DC anode power is delivered across the body of the PSDS heated by MgO-insulated AC cartridge heaters. Due to the high probability for component failure, the control system was custom-built to utilize modular, readily available components for easy replacement. A diagram of the control system is shown in Fig 9. An arduino is used to receive thermocouple data and to drive via 3 software PIDs a pair of two-channel triodes for alternating current (TRIACs) via a standard DMX interface for ease of integration. One TRIAC controls the propellant while the other controls the pair of tank heaters. An AC power meter measured power consumption and a filter was used to prevent TRIAC feedback on the line. The compact control system is shown in Fig 10 during PSDS operation.

Temperature measurements were taken with Type-K and Type-J thermocouples that are encapsulated in the cartridge heaters. Auxiliary mineral-insulated Type-K thermocouples were used to measure wall temperatures. MCP9600 thermocouple amplifiers have been used due to their performance and electrostatic discharge protection (ESD).
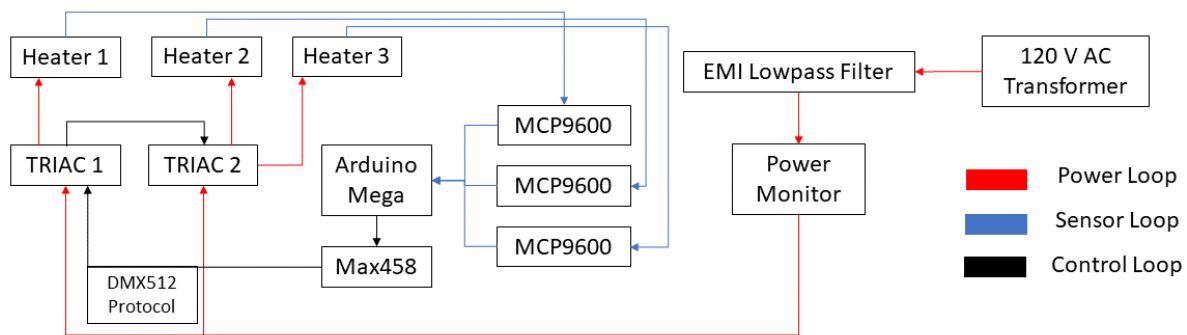

Fig. 9 PSDS control circuit schematic.

Propellant output was obtained through mass measurements before and after the experiments. The Mark 3 PSDS was weighed using an Ohaus Adventurer analytical balance 320g/0.1 mg shown in Fig 11 before and after experiments.

The Zinc slugs used in experiments were machined down from 16 mm outer diameter to 15 mm diameter to remove the tarnished and oxidized surface layers. A selected slug was loaded into the PSDS and the heaters were connected. Mass measurements of the fully assembled PSDS were taken. The PSDS was then connected to the thruster and assembled in the vacuum chamber for testing. A mixture of "thruster-on" and "thruster-off" propellant output measurements were taken at approximately 7e-5 mbar chamber pressure. PSDS assembly mass was measured post-test without removing the propellant slug or any heaters for measurement consistency. The flow rate was estimated using the recorded temperature profile and the flow model.

Fig. 10   Mark 3 PSDS control system (top) and thruster DC power supply (bottom).
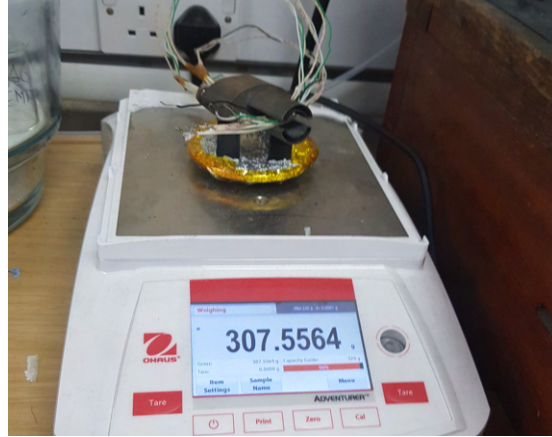
Fig. 11   Mass measurement of the Mark 3 PSDS before the experiment.

E. Experimental Results and Propellant Output

Table 1 summarizes the operational window of the Mark 3 PSDS on zinc. The temperature was varied from approximately 390 ° C to 450 ° C, while the total sublimation duration was kept between 15 to 35 minutes. The zinc flowrate ranged from 0.14 mg/s (3 SCCM) to 0.36 mg/s (7.5 SCCM) in sublimation mode and up to 8.23 mg/s (169 SCCM) when the propellant temperature was allowed to exceed the melting temperature. Experiment 8 and 9 were undertaken back-to-back with a melted propellant slug. Experiments 1 to 7 were performed in sublimation mode.

Table 1   Measured Zinc Propellant Output of the PSDS Mark 3.

Experiment	Total Sublimation Time, min	In Operation Sublimation Time, min	Target Temperature, C	PSDS Mass Loss, mg	Sustained Flow Rate, mg/s	Sustained Flow Rate, SCCM
1	33.33	17.99	393	239.5	0.1489	3.064
2	35.62	22.02	408	350	0.2365	4.865
3	20.51	7.90	385	205.4	0.2437	5.012
4	22.58	7.70	409	298.1	0.2721	5.596
5	18.36	4.90	413	351.6	0.3256	6.696
6	27.56	19.51	408	410	0.3404	7.002
7	37.71	18.44	422	767.6	0.3623	7.452
8	15.55	10.81	442	11640	5.8989	121.339
9	36.13	14.22	452		8.2358	169.407

The Mark 3 PSDS zinc output was consistent and repeatable. The generated zinc flow was sufficient for the ignition and sustained operation of a 100 W cylindrical Hall thruster which requires 5 to 10 SCCM of xenon. Due to the low achievable pressure differential, sublimated zinc propellant transport is heavily limited by the available cross-sectional area. Given the physical dimensions of the 100 W cylindrical Hall thruster discharge channel, the performance of the PSDS on zinc is limited to a flowrate of 8 SCCM at temperatures below the melting temperature of the propellant. As the size of the thruster is increased, larger PSDS cross-sectional areas are possible leading to higher propellant flow rates in sublimation mode. Magnesium, on the other hand, can achieve a much higher vapor pressure through sublimation and does not experience the same limitation as zinc. Consequently, different propellants can lead to different performance in the same PSDS.

Results from operation on the zinc propellant slug were similar compared to previous experiments [18]. The surface of the zinc slug is shown in Fig 12 before and after a test, illustrating the formation of a crystalline structure on the surface of the zinc. Localisation at the tip of the slug of deformations to the slug shape as a result of sublimation are most likely due to the distribution of resistive heater windings within the cartridge heater.

8

Fig. 12   Propellant slug before and after a test.

Fig. 13   Condensation during cool down.

Condensation within the Mark 3 PSDS can be controlled depending on the operational mode chosen. The PSDS can operate with wall temperatures above the melting point (>420 ° C) to prevent condensation inside the tank. Alternatively the walls and the propellant can be driven at the same temperature allowing condensation to occur on the walls, as shown in Fig 13. Regardless, the walls can be purged by heating the tank above 420 ° C. The hollow anode represents the key to this PSDS design. No heater is used to heat up the hollow anode and as a result condensation occurs. Grey zinc deposition on the hollow anode with no plasma discharge is shown in Fig 14 during the start-up phase. Despite the condensation, sufficient zinc output is measured to allow the ignition of the thruster even with losses to the walls as shown in Table 1. Once ignited, the residual heat from the anode purges the condensed zinc, briefly increasing propellant output. Afterwards the propellant flow rate is stabilised in steady-state operation. The hollow anode is shown in Fig 15 after successful ignition of the thruster. In this case it is observed that if the sublimation rate is high enough to cover losses, zinc deposition on the walls does not critically impact the flow rate. Should deposition increase to the extent of obstruction, tank heater power can be increased to fully purge the propellant lines (estimated power for purge of the entire system is 100 W).

**Fig. 14   Hollow anode condensation - thruster OFF.**

Fig. 15   Hollow anode condensation - thruster ON.

IV. Cylindrical Hall Thruster Modification - CHT-Zn

A. Original CHT-100 Design

The preliminary test platform for alternative propellants was a low power cylindrical Hall thruster (CHT-100) [23]. It features a conventional design [24] and was constructed to operate in the 100 W - 300 W range. It can operate in either permanent magnet or electromagnet mode due to the modular design. For this series of experiments, the thruster was operated in electromagnet mode with a small, 110-turn solenoid as the secondary coil and a large, 560-turn solenoid as the primary coil. The annular section has an inner diameter of 15 mm, an outer diameter of 27 mm and a depth of 18.5 mm with a total channel length of 38.5 mm. The anode is of a conventional gas distribution design with a single

3.175 mm feed and its inclusion alters the channel length to 9.5 mm for the annular section and 29.5 mm in total. A schematic of the CHT-100 is shown in Fig. 16.
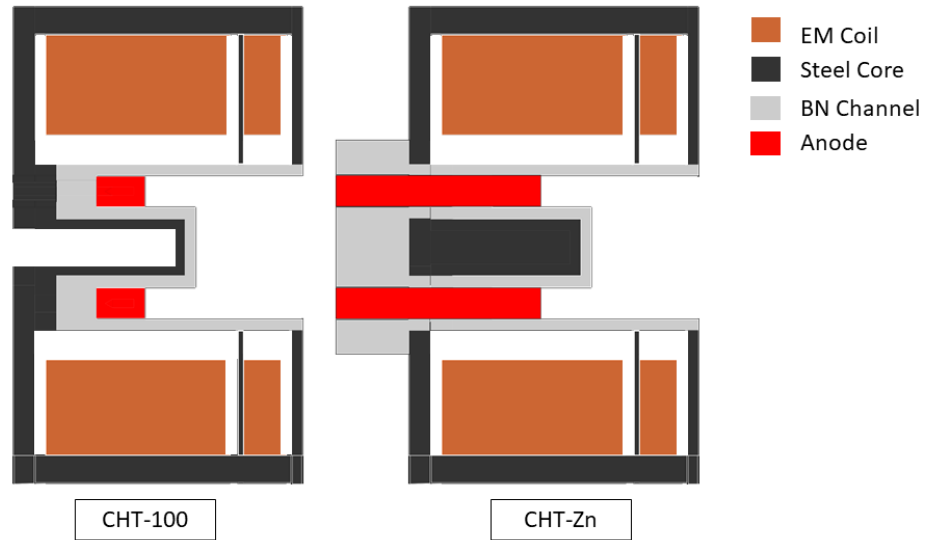

Fig. 16   CHT-100 vs CHT-Zn schematic.

B. Modified CHT-Zn Design

Due to the high cross-sectional area required by zinc to overcome the limited vapor pressure differential, and the hollow anode feed design, the CHT-100 was modified to permit coupling with the Mark 3 PSDS. The modified cylindrical Hall thruster was named CHT-Zn. A cross-sectional view of the Mark 3 PSDS - CHT-Zn is shown in Fig 17. The modifications were limited to the channel, pole and back plate. The back plate, shown in Fig 18, was machined to connect the central pole through two thin bridges of ferromagnetic steel that provide sufficient structural support . It is possible to increase the cross-sectional area of the hollow anode by using a single ferromagnetic bridge connection to the pole for a U shaped hollow anode or a ferromagnetic pole attached directly to the PSDS for a completely annular hollow anode.
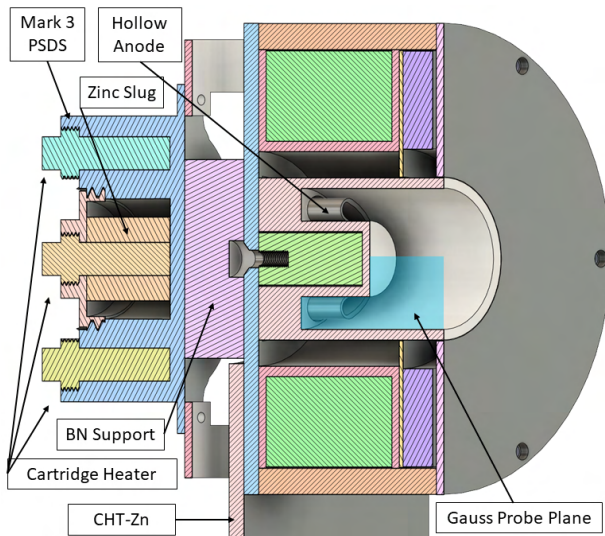
Fig. 17   CHT-Zn cross-section CAD.
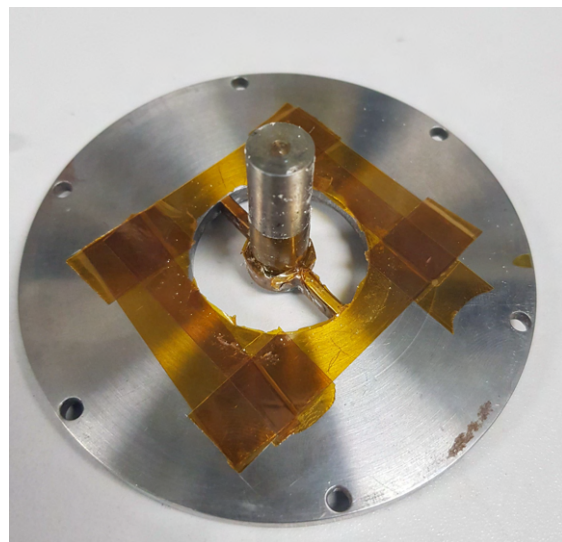
**Fig. 18   CHT-Zn back plate with central pole.**

The Mark 3 PSDS was inserted with the hollow anode between the two bridge sections on the ferromagnetic CHT-Zn back plate, as shown in Fig 17. To accommodate the hollow anode geometry, the ceramic channel of the thruster was reconstructed from boron nitride with large semicircular slots. The inner diameter of the annular section of the channel was reduced to 14.5 mm and the outer diameter was kept at 27 mm while two oval slots were clearance cut according to the anode shape. A 0.5 mm clearance was included in the channel slots to allow for anode deflection and thermal expansion. A secondary support was used to prevent plasma leakage and to shield the open back plate bridge sections. Both the support and the channel were manufactured from boron nitride. As the PSDS was also the anode of the thruster, two ceramic plates were used to mechanically connect the PSDS to the thruster body, providing electrical insulation between the thruster body and the PSDS. An advantage of this connection method is that the length of the discharge channel can be varied depending on the dimensions of the ceramic brackets and support piece. In addition, the hollow anode acts as an artificial channel extension. This may be beneficial in the case of thruster operation on magnesium because magnesium has a larger mean free path.

Thermally, the PSDS with its hollow anode is almost completely decoupled from the thruster, isolated through spatial clearance with conduction paths localised to bolted connection points. This represents an advantage since the solenoids are less temperature-constrained and can be operated at a higher power. At the same time, the PSDS is more thermally constrained, although this is advantageous as the excess heat is concentrated on the propellant feed to prevent condensation, eliminating the need for additional heaters.

Finally, the Mark 3 PSDS was designed to allow thruster operation on gaseous propellant. This is achieved through a modified propellant cartridge heater support that connects to a Swagelok compatible intake. In this configuration, the gas is pushed through the same geometry as the zinc. This enables a comparison of performance during operation with solid vs gaseous propellants.

C. CHT-Zn Magnetic Field

The structural changes in the CHT-Zn result in a different magnetic circuit, due to the large cut-outs in the thruster's ferromagnetic back plate. The unique field topology was modeled with FEMM assuming complete decoupling of the pole from the body for axisymmetry. The results of the simulation are shown in Fig 19 with 0.8 A applied to the main coil and 1 A applied to the secondary coil. The current limits represent the chosen testing condition for zinc to allow self ignition and reduce complexity by eliminating the risk of electromagnets extinguishing the plasma discharge. Yet the deliberately chosen solenoid parameters do not represent the peak performance window of the CHT-Zn. Previous experiments showed peak efficiencies in the CHT-100 at roughly 1.5 A to 2 A in both solenoids. The decoupled pole creates a nearly Hall thruster-like radial magnetic field at the back of the CHT-Zn, shown in Fig 19. A boron nitride support piece was designed to extend the discharge channel and block plasma from escaping the discharge channel at the back plate.
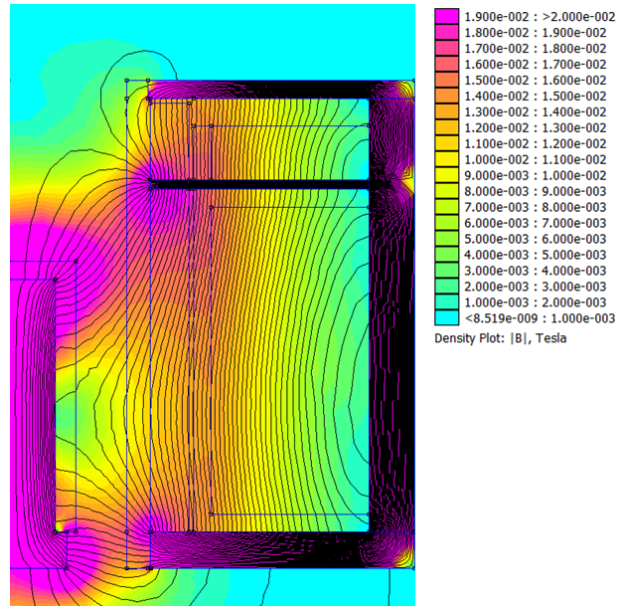

Fig. 19   CHT-Zn FEMM axisymmetric model 0.8 A - main coil 1 A - secondary coil.

The design of the CHT-Zn axially towards the exit is unchanged from the original cylindrical Hall thruster design. The magnetic flux density of the original CHT-100 was measured and compared to the flux density of the CHT-Zn at the same coil current. A GM08 gaussmeter was mounted on an automated Thorlabs translation stage as shown in Fig 17. Magnetic field measurements are shown in Fig 20 and 21. As expected, the peak field strength in the CHT-100 is higher than that of the CHT-Zn by approximately 50 G. While the sensor location on the probe limited the number of accessible measurement locations above the pole, the data are considered sufficient to conclude a good similarity between the magnetic field topology of the two thrusters.

A second investigation of interest is to confirm the validity of the axisymmetric assumption in the FEMM simulation, given the non-axisymmetric nature of the CHT-Zn ferromagnetic back plate which connects the ferromagnetic pole via

two thin metallic bridges, as shown in Fig 18. The flux density of the CHT-Zn was measured in two orthogonal planes, one plane into the metallic bridge and one plane where there is no connection between the pole and the structure. The results are shown in Figs 22 and 23. The field topology is almost identical with a 20 G increase in strength near the pole in the bridge plane. Axisymmetry is therefore considered a good assumption.
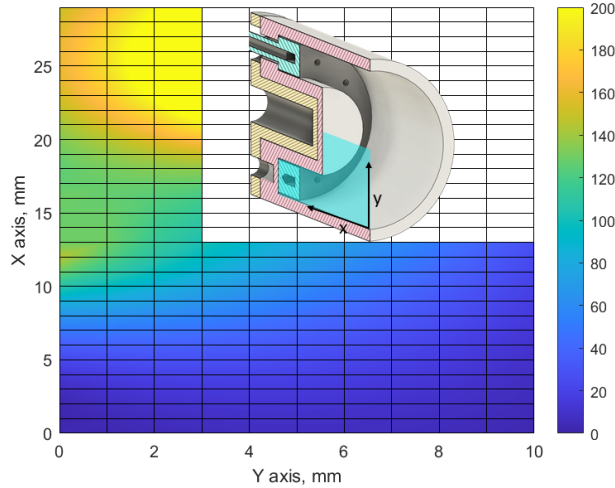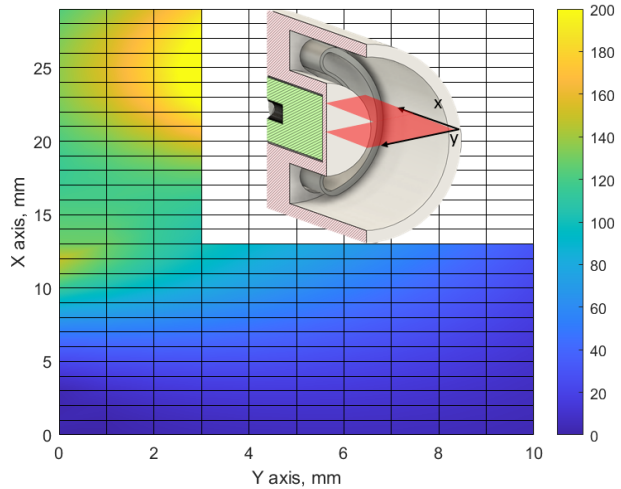

Fig. 20 CHT-100 magnetic flux density 0.8 A - 1 A - peak strength 250 G.
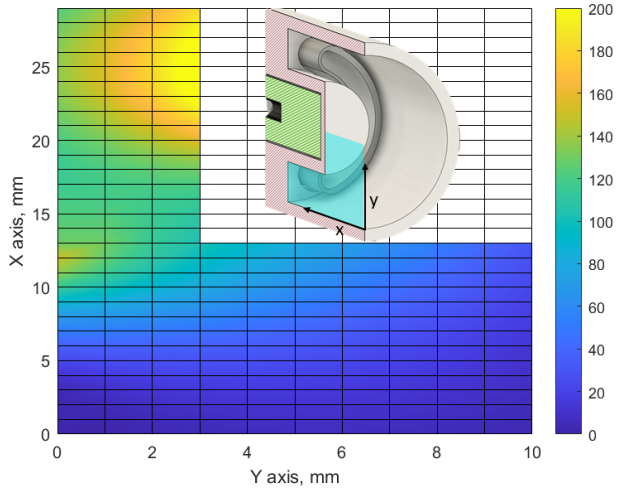
Fig. 21 CHT-Zn magnetic flux density 0.8 A - 1 A - peak strength 200 G.
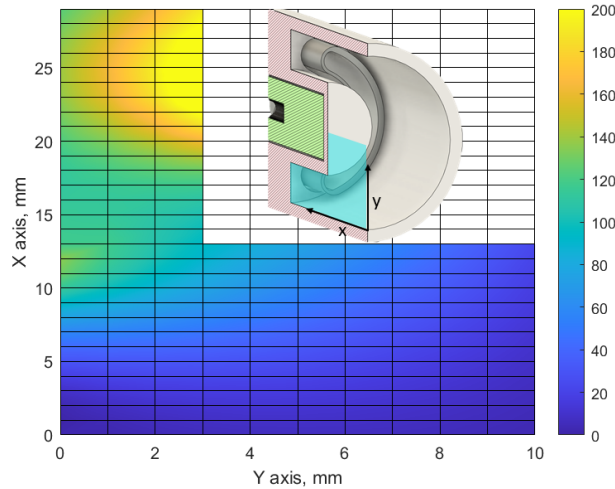
Fig. 22 CHT-Zn magnetic flux density bridge plane 0.8 A - 1 A - peak strength 220 G.

Fig. 23 CHT-Zn magnetic flux density clear plane 0.8 A - 1 A - peak strength 200 G.

No abnormal plasma formations were identified as a result of the asymmetric propellant injection through the hollow anode during CHT-Zn operation, as shown in Fig. 24. The presence and uniformity of the central spike suggests that the magnetic field topology of a cylindrical Hall thruster has been successfully retained in the CHT-Zn.


Fig. 24 CHT-Zn channel during operation.

V. CHT-Zn Performance Measurements

A. Experimental Setup and Equipment

The CHT-Zn thruster and the Mark 3 PSDS were tested in the David Fearn Electric Propulsion Facility at the University of Southampton. The main vacuum chamber is 2 m in diameter and 4 m long. The chamber is equipped with a roughing pump, 2 turbo pumps, and two cryogenic pumps providing a base pressure of 7e-8 mbar with no gas flowing into the chamber. An operational pressure on the order of 1.1e-5 mbar to 1e-6 mbar is achieved with a flowrate of 10 SCCM of xenon into the chamber. The cathode used is a Model 5000 Hollow cathode electron source supplied by IntlVac which can provide 0-20 A. The design is based on tungsten filament electron emission and is shown in Fig 25. The cathode was designed for laboratory work and requires higher propellant flow rates than space-grade cathodes. Therefore it is not included in total efficiency calculations. The cathode was operated primarily with krypton and xenon at flowrates up to 3 SCCM. Excessive cathode flow caused a glowing effect on the CHT-Zn and a high-voltage, low-current plasma bridge when the anode was energised with zero mass flowrate. To eliminate ingestion concerns, the cathode flowrate was reduced to a minimum stable flow output which eliminated the anode connection and the induced glow.
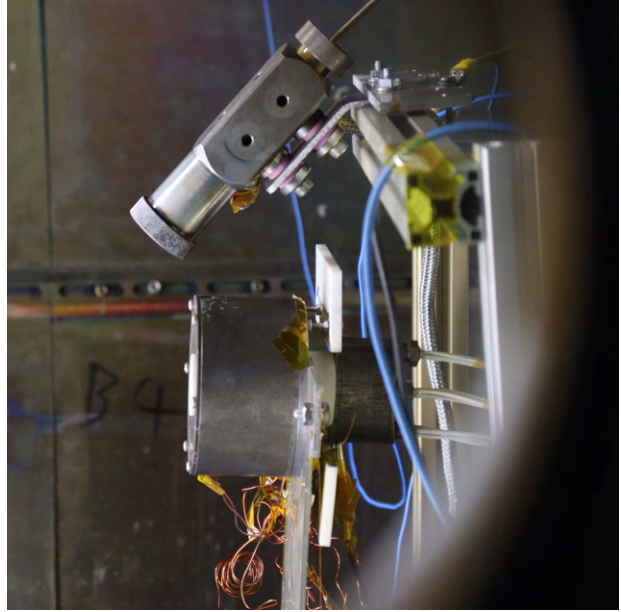

Fig. 25   CHT-Zn - Mark 3 PSDS and Model 5000 cathode on thrust stand.

The CHT-Zn was tested on a hanging pendulum thrust balance, shown in Fig 27. Displacement was measured with a Micro-epsilon 1700 laser triangulation sensor. To convert the displacement to thrust, a Thorlabs linear displacement stage was integrated into the thrust balance. Using an automated stepping program with 2.5 mm increments, a 4.717 g weight was driven to simulate a known load on the system. An example of the resulting calibration fit is shown in Fig 26 from which the calibration factor α is extracted. Due to the need to mechanically remove the thruster for flow rate estimation, calibration was performed prior to every experiment for consistent results. To protect the pumping system, a stainless steel mesh trap was used in conjunction with a stainless steel beam dump.
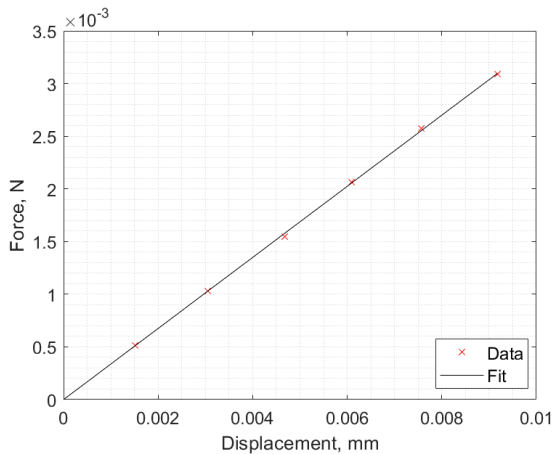
Fig. 26   Example force-displacement calibration fit for the pendulum thrust stand.
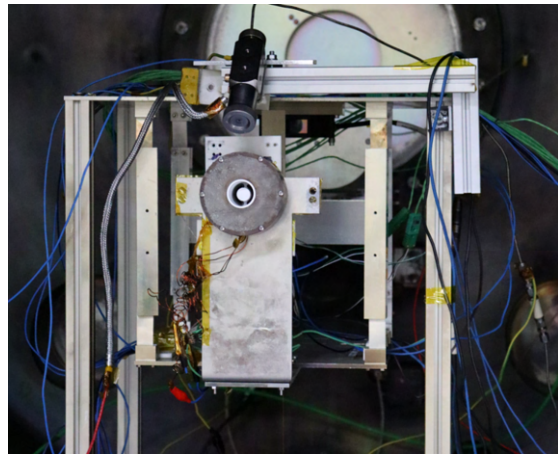
Fig. 27   Hanging pendulum thrust stand in the vacuum chamber.

B. Methodology

Thrust measurements are obtained from the displacement jump when the thruster discharge is extinguished. Specific impulse is calculated using the propellant flow rate, which is either set by a Bronkhorst flow controller for xenon and krypton or calculated from the temperature profile and mass measurements for zinc. Thruster anode efficiency is then calculated using voltage and current measurements from the power supply. In this case the anode efficiency is the only efficiency calculated. The following equations are used to evaluate the performance of the thruster:

$$F = \alpha \delta_d \qquad (6)$$

$$Isp = \frac{F}{g_0 \dot{m}_p} \qquad (7)$$

$$\eta_a = \frac{F^2}{2 P_a \dot{m}_p} \qquad (8)$$

C. Zinc Performance

The CHT-Zn was successfully fired and tested on zinc. To the best of the authors knowledge this marks the first documented use of zinc in a cylindrical Hall thruster. To the best of the authors knowledge this also marks the first use of zinc in the Hall thruster class below 100 W. Images of the thruster plume are shown in Figs 28 and 29. The color of the plume shifted significantly when power was applied to the electromagnets, as shown in Fig 28. A summary of performance data is shown in Table 2. Experiments 1 to 4 and 7 were performed in sublimation mode while 5 and 6 were performed in melting mode to demonstrate the limits of the system. Experiment 7 is a unique experiment involving a mixture of zinc (0.122 mg/s) and krypton (0.3116) to a ratio of 2.5 SCCM zinc to 5 SCCM krypton, which achieved operation at very low anode power (39 W). The CHT-Zn anode power was varied between 39 W to 85 W with an anode voltage between 50 V to 107 V. The resulting thrust was between 0.7 mN up to 1.2 mN with a peak specific impulse of 448 s at 82.36 W. Efficiencies are low, given that the CHT-Zn operation was not optimised, yet the range 1.38% to 2.77% for zinc is comparable to xenon and krypton at the same testing parameters. The parasitic power required by the heating system was not included in the efficiency calculation. The PSDS operational power cost was 20-30 W during thruster operation. The power cost can be reduced further through radiation shielding and operation at a higher discharge power.

Fig. 28 Plume of the CHT-Zn on zinc: (up) electromagnets off; (down) electromagnets on;
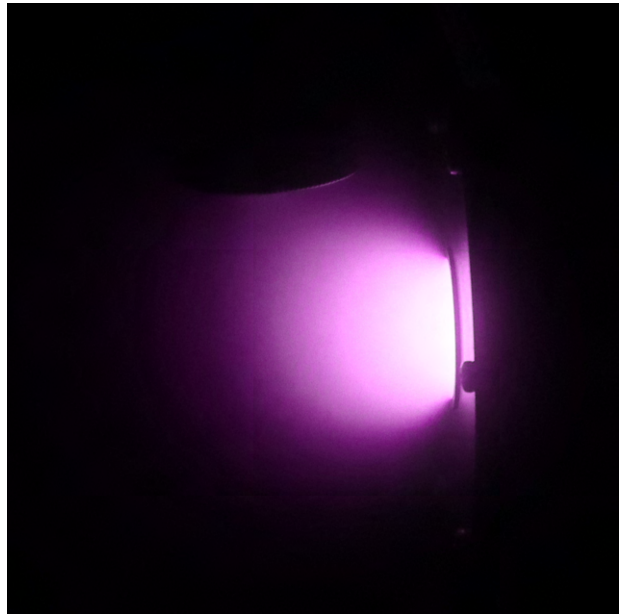
**Fig. 29 Plume of the CHT-Zn on zinc - variable ND 64-1000 filter.**

Table 2   Summary of CHT-Zn performance on zinc at 0.8 A main coil - 1 A secondary coil.

| Index	Voltage, V	Current, A	Power, W	Flow Rate, mg/s	Flow Rate, SCCM	Thrust, mN	Isp, s	Efficiency, %
1	85.0	0.700	59.50	0.3533	7.267	0.8557	246.99	1.7418
2	93.0	0.700	65.10	0.3683	7.576	0.9215	255.13	1.7709
3	80.9	1.059	85.67	0.2202	4.529	0.7241	335.33	1.3896
4	107.8	0.764	82.36	0.2365	4.865	1.0400	448.35	2.7761
5	80.0	1.000	80.00	8.0021	164.600	1.0874	13.86	0.0924
6	58.7	1.068	62.69	5.2520	108.031	1.1966	23.23	0.2175
7*	50.0	0.787	39.35	0.4340	7.519	0.7773	182.63	1.7689

D. Xenon Performance

Operation of the same thruster geometry on xenon was examined between 55 W to 156 W with an anode voltage between 80 V to 132 V. The resulting thrust was between 1 mN up to 3.1 mN with a peak specific impulse of 450 s
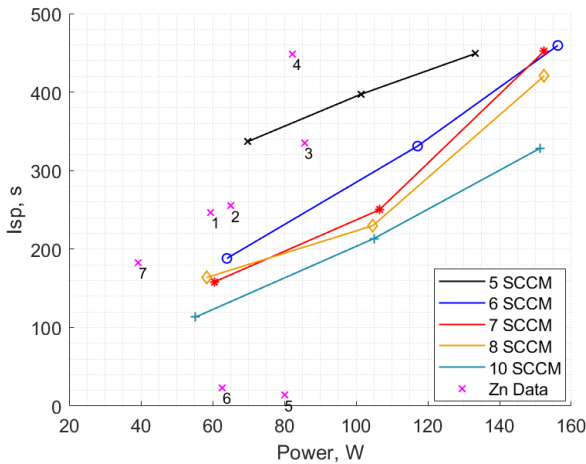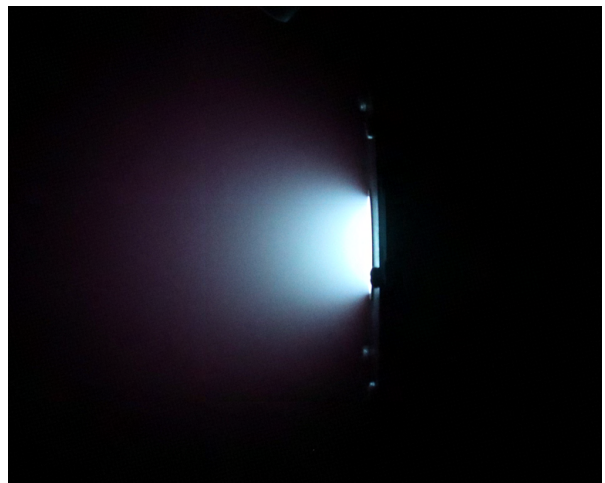

Fig. 30   Specific impulse vs anode power Xe vs Zn.
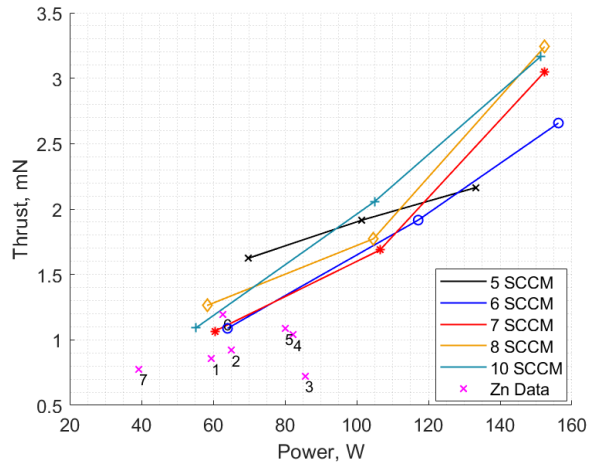
Fig. 31   Thrust vs anode power Xe vs Zn.
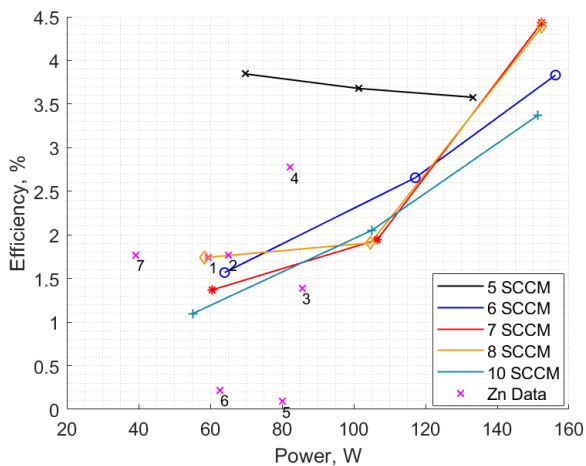
Fig. 32   Efficiency vs power Xe vs Zn.

Fig. 33   Plume of the CHT-Zn on xenon.

15

at 156.24 W. The anode efficiency ranged from 1.09% to 4.43%. Performance data are shown in Figs 30, 31, and 32 together with the zinc measurements presented in Table 2. The xenon plume of the CHT-Zn is shown in Fig 33.

E. Krypton Performance

Krypton was tested to generate a second dataset with the same geometry. The power range was 52 W to 147 W with an anode voltage between 80 V to 132 V. The resulting thrust was between 0.9 mN up to 2.6 mN with a peak specific impulse of 689 s at 143.19 W. The anode efficiency ranged from 0.64% to 5.43%. Performance data are shown in Figs 34, 35, and 36 together with the zinc measurements presented in Table 2. The krypton plume of the CHT-Zn is shown in Fig 37.
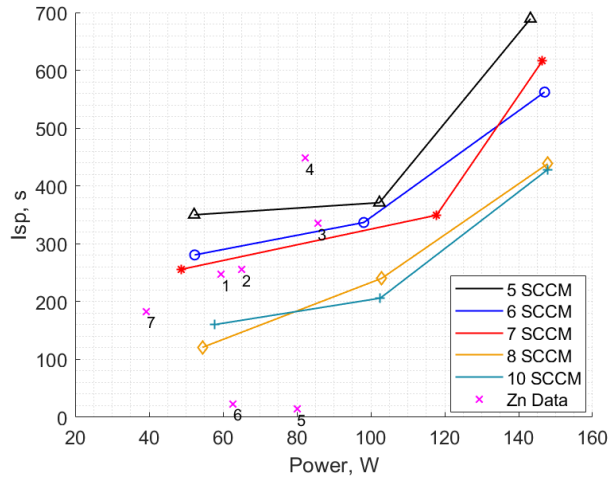

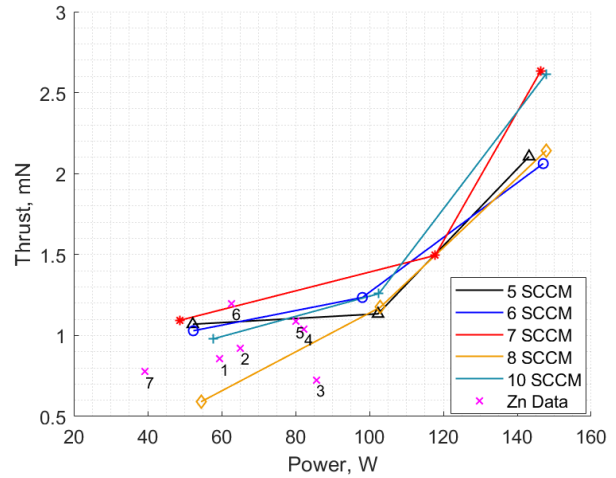Fig. 34   Specific impulse vs anode power Kr vs Zn.

Fig. 35   Thrust vs anode power Kr vs Zn.
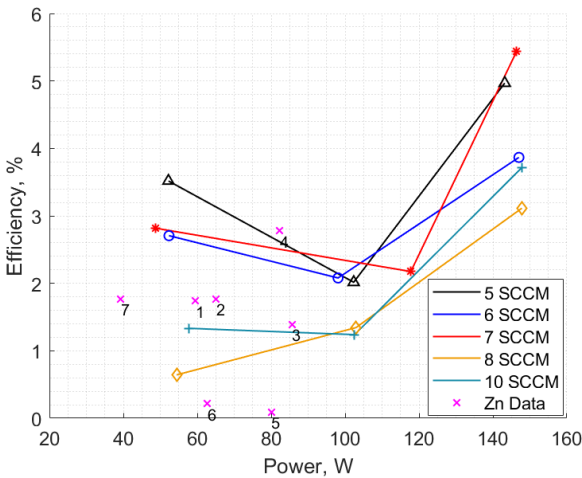
Fig. 36   Efficiency vs power Kr vs Zn.
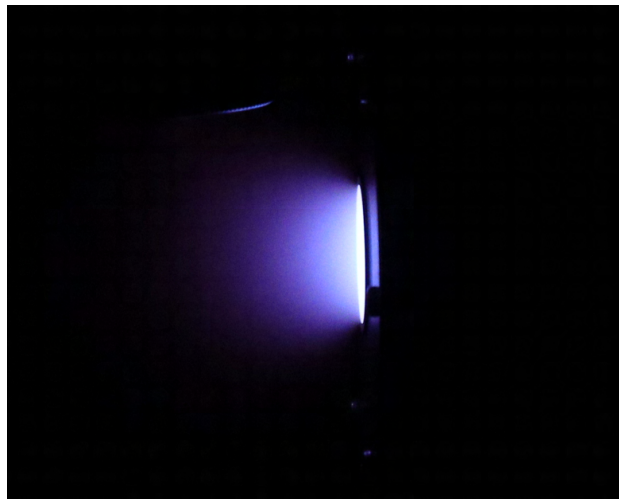
Fig. 37   Plume of the CHT-Zn on krypton.

VI. Performance Review and Discussion

Overall zinc shows good performance comparable to xenon and krypton at much lower anode power when considering the low coil current used. Even when adjusting the data by 20-30 W to include the heating power loss, the thrust and Isp still match that of operation on krypton. Considering the difference in density between zinc (7.13 g/cm^3) and pressurised krypton (approximately 0.5 g/cm^3) it becomes clear that zinc is a preferred alternative to xenon. These

16

results are consistent with previous findings [9] that suggest a potential for a high specific impulse for operation on zinc. With the ability to run at low discharge voltages and powers, zinc may be a good competitor to xenon in the low- to medium-thrust satellite propulsion subsystem market. A few key findings of this paper follow in the discussion.

A. Ignition, Throttle, Redundancy

The CHT-Zn was operated in current-limited mode for xenon, krypton and zinc as a direct consequence of the low coil currents. Igniting the thruster was relatively easy with zinc and occurred almost instantly after applying 200 V and 0.7 A to the anode when there was a propellant output of approximately 5-6 SCCM of zinc. Aggressively changing the coil current resulted in the plasma being extinguished. Therefore, the coil current was limited to relatively low values for this initial testing. Thruster ignition was highly sensitive to cathode position with xenon, krypton and zinc.

Throttling of the thruster was also demonstrated on zinc by varying the output flow rate. The throttling flow rate behavior is illustrated in Fig 38 where the temperature of the core was reduced in two consecutive 2° C increments which reduced the flow by approximately 0.025 mg/s at each step (0.5 SCCM). Consequently, the voltage in current-limited mode was lower when all other test parameters were held constant. The thermal isolation of the propellant core in the PSDS design allows for sufficient flow rate control by temperature adjustment alone.

To demonstrate a failure mode operation, power was intentionally removed from the propellant core heater and only the thermocouple within the core heater was used to measure the propellant temperature. The tank heaters were controlled with external thermocouples (replicating internal thermocouple failure) at a higher temperature / power to indirectly control propellant temperature and compensate for the simulated propellant heater failure. Control system failure was simulated by limiting the current in the AC heaters such that the total output power was 70 W, and by turning off the PID control. Despite these limitations, thruster operation was still possible on zinc. The estimated flow rate is shown in Fig 39. Without PID control and excess tank heating, upon thruster ignition the temperatures in the system increased by approximately 40-60 °C at the measurement point represented by the 5 consecutive spikes in flow rate (shown in Fig 39). While the thruster ON-time was limited in this case to a few short operational bursts of a few minutes each to prevent melting, the robustness of the system in adverse operating conditions is considered demonstrated.

In this operational mode, thruster shutdown was attempted by eliminating the heater power (cooling the PSDS) while maintaining anode power and a plasma discharge. Surprisingly, the propellant temperature stabilised during thruster operation and the tank temperature began dropping slowly. Given the slow rate of wall cooling, it was estimated that below a certain temperature threshold, the lower tank temperature would suppress gaseous propellant generation by forcing heavy condensation. Due to time constraints the experiment was stopped before the walls could cool sufficiently.
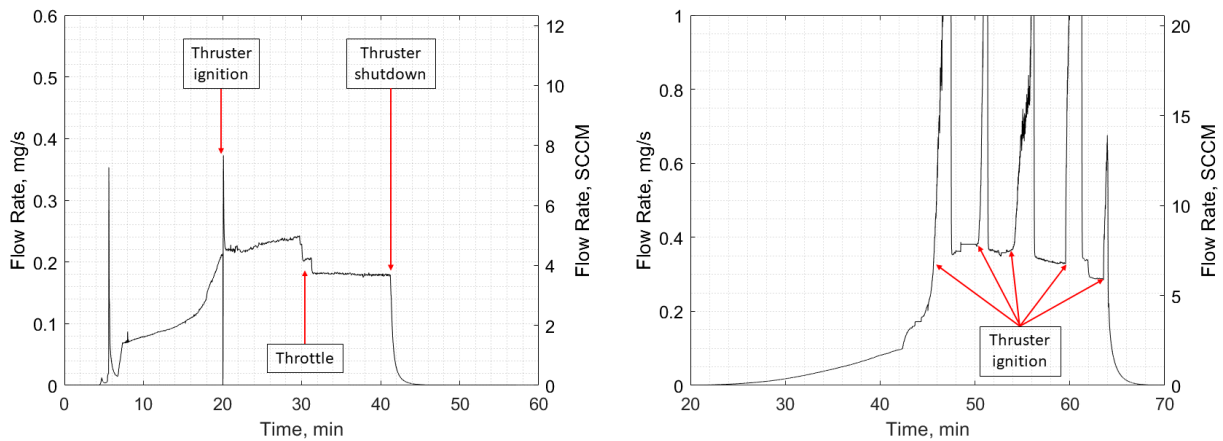
Fig. 38   Estimated zinc flow rate - full control mode. Active throttling at the 30 min mark.

Fig. 39   Estimated zinc flow rate - heater/PID failure simulation mode.

B. Channel Erosion and Propellant Deposition

Another novelty of this project is the investigation of channel deposition and erosion which began with this experimental campaign. In this laboratory model of the thruster, the discharge channel can be detached and reattached

Table 3   Summary of CHT-Zn channel mass measurements (* thruster off).

Zinc Experiment	Peak Sustained Flow, SCCM	Propellant Output Time, min	Channel Mass Gain, mg
1	7.45	18.44	201.7
2*	6.70	4.90	12.5
3*	5.60	7.70	8.5
4	2.50	17.99	9.5
5*	5.01	7.90	5.7
Xenon Experiment			
1	5-10	86	-3.1
Krypton Experiment			
1	5-10	43	-12.2

easily, allowing for mass measurement after each experiment. Three boron nitride channels have been produced with one used exclusively for zinc, one for gasses such as krypton or xenon, and one to be used for magnesium. The mass measurements are summarised in Table 3. Zinc experiments(*) 2,3 and 5 were made with the thruster turned OFF while the other experiments were completed with the thruster turned ON, in the presence of a thruster discharge.

Thruster operation on xenon and krypton led, as expected, to mass loss during thruster firing, indicating erosion of the channel.

Zinc testing showed increasing discharge channel mass with both the thruster OFF and ON. When zinc gas was exhausted from the PSDS without a discharge, the deposition rate was relatively low and with only superficial propellant attachment to the surface of the channel. Experiment 4 shows the effect of using a zinc and krypton mixture (2.5 SCCM zinc / 5 SCCM krypton). In this case, the zinc deposition on the channel was thin yet firmly attached to the channel structure, forming a protective coating. While the zinc coating with the thruster OFF can be easily removed by wiping the surface, the coating with the thruster ON is not easily removed and the surface must be scored, suggesting firm attachment. Thruster operation at a higher zinc mass flowrate, as in the case of experiment 1, substantially increased the amount of deposited zinc. The zinc deposition was again firmly embedded in the channel. In this case, no gas purging mechanism was installed and the leftover zinc gas inside the channel cooled and formed into small granules that affected measurements. Images of the channel in different stages are shown in Fig 40. It should be noted that the fine layer of zinc was electrically conductive but not in any close proximity to sensitive conductive surfaces or at a risk of forming a bridge between other thruster components (e.g. anode and thruster body), even with extended operation use.

The evidence presented, although restricted to results from a limited number of tests, suggests that it may be possible to avoid channel erosion when using metallic propellants. Mixtures of metals and gasses could also work in regeneration cycles. Further investigation will be undertaken to provide a thorough analysis of this unique behavior.

Fig. 40   Channel deposition: (left) new channel; (middle) deposition with krypton and zinc mixture; (right) deposition after sustained zinc operation;

Zinc deposition on the external body of the thruster and auxiliary support structure was observed. However, it is speculated that it was a result of beam reflection from a stainless steel beam dump used to protect sensitive equipment because the deposition pattern was localised at positions corresponding to reflective angles from the beam dump surface. This was further reinforced by a lack of deposition in the geometric shadow of thruster elements. The zinc deposition

was localised on steel and kapton-covered surfaces with minimal to no deposition on aluminium and stainless steel components.

VII. Conclusion and Upcoming Work

A unique propellant storage and delivery system for solid, condensable propellants was built and successfully tested with zinc. An existing 100 W cylindrical Hall thruster (CHT-100) was modified and adapted for zinc testing (CHT-Zn). The thruster was operated with zinc, xenon and krypton and the performance data were presented. Zinc was shown to provide a similar performance to krypton at a lower anode power. The specific impulse observed during operation on zinc was higher compared to the specific impulse observed during operation on xenon and krypton at the same anode power. Consequently, through the collected experimental data, zinc is recommended for usage even at lower powers in sub kW class thrusters due to the advantageously high propellant density, low cost and relatively low required parasitic heater power. Condensation and channel erosion are discussed and the potential for channel regeneration is highlighted through experimental data.

Upcoming experimental work will focus on demonstration of higher performance for operation of the CHT-Zn on zinc and the performance characterisation of magnesium. A unique annular Hall thruster (HA-Zn-HET) has been developed and manufactured for operation on zinc, magnesium, xenon and krypton featuring a hollow anode configuration and variable magnetic field topology with an external scaled-up version of the PSDS presented here (Mark 4 PSDS). This will enable performance measurements at higher input powers (330 W - 400 W) and optimisation of the field topology for operation on zinc and magnesium.

Acknowledgments

References

[1] Lev, D., Myers, R. M., Lemmer, K. M., Kolbeck, J., Koizumi, H., and Polzin, K., "The technological and commercial expansion of electric propulsion," *Acta Astronautica*, Vol. 159, 2019, pp. 213–227. https://doi.org/https://doi.org/10.1016/j.actaastro.2019.03.058.

[2] Rafalskyi, D., Martínez, J. M., Habl, L., Zorzoli Rossi, E., Proynov, P., Boré, A., Baret, T., Poyet, A., Lafleur, T., Dudin, S., et al., "In-orbit demonstration of an iodine electric propulsion system," *Nature*, Vol. 599, No. 7885, 2021, pp. 411–415. https://doi.org/https://doi.org/10.1038/s41586-021-04015-y.

[3] Kieckhafer, A., and King, L. B., "Energetics of Propellant Options for High-Power Hall Thrusters," *Journal of Propulsion and Power*, Vol. 23, No. 1, 2007, pp. 21–26. https://doi.org/https://doi.org/10.2514/1.16376.

[4] Glueckauf, E.-N., and Kitt, G., "The krypton and xenon contents of atmospheric air," *Proceedings of the Royal Society of London. Series A. Mathematical and Physical Sciences*, Vol. 234, No. 1199, 1956, pp. 557–565. https://doi.org/https://doi.org/10.1098/rspa.1956.0057.

[5] Herman, D. A., and Unfried, K. G., "Xenon Acquisition Strategies for High-Power Electric Propulsion NASA Missions," *JANNAF SPS Subcommittee Meeting*, 2015.

[6] Szabo, J., Robin, M., and Hruby, V., "Bismuth Vapor Hall Effect Thruster Performance and Plume Experiments," *Proceedings of the the 35th International Electric Propulsion Conference*, 2017, pp. 2017–25.

[7] Szabo, J., Pote, B., Paintal, S., Robin, M., Hillier, A., Branam, R. D., and Huffmann, R. E., "Performance Evaluation of an Iodine-Vapor Hall Thruster," *Journal of Propulsion and Power*, Vol. 28, No. 4, 2012, pp. 848–857. https://doi.org/10.2514/1.B34291.

[8] Polzin, K. A., "Iodine Hall thruster propellant feed system for a CubeSat," *50th AIAA/ASME/SAE/ASEE Joint Propulsion Conference*, 2014, p. 3915. https://doi.org/10.2514/6.2014-3915.

[9] Szabo, J., Robin, M., Duggan, J., and Hofer, R. R., "Light metal propellant Hall thrusters," *31st International Electric Propulsion Conference*, 2009, pp. 2009–138.

[10] Hopkins, M. A., and King, L. B., "Magnesium Hall Thruster with Active Thermal Mass Flow Control," *Journal of Propulsion and Power*, Vol. 30, No. 3, 2014, pp. 637–644. https://doi.org/10.2514/1.B34888.

[11] Makela, J. M., Washeleski, R. L., Massey, D. R., King, L. B., and Hopkins, M. A., "Development of a Magnesium and Zinc Hall-Effect Thruster," *Journal of Propulsion and Power*, Vol. 26, No. 5, 2010, pp. 1029–1035. https://doi.org/10.2514/1.47410.

[12] Jacobson, D., and Manzella, D., "50 kW class krypton Hall thruster performance," *39th AIAA/ASME/SAE/ASEE Joint Propulsion Conference and Exhibit*, 2003, p. 4550. https://doi.org/10.2514/6.2003-4550.

[13] Shabshelowitz, A., Gallimore, A. D., and Peterson, P. Y., "Performance of a Helicon Hall Thruster Operating with Xenon, Argon, and Nitrogen," *Journal of Propulsion and Power*, Vol. 30, No. 3, 2014, pp. 664–671. https://doi.org/10.2514/1.B35041.

[14] Fujita, D., Kawashima, R., Ito, Y., Akagi, S., Suzuki, J., Schönherr, T., Koizumi, H., and Komurasaki, K., "Operating parameters and oscillation characteristics of an anode-layer Hall thruster with argon propellant," *Vacuum*, Vol. 110, 2014, pp. 159–164. https://doi.org/https://doi.org/10.1016/j.vacuum.2014.07.022.

[15] Schwertheim, A., and Knoll, A., "Low power thrust measurements of the water electrolysis Hall effect thruster," *CEAS Space Journal*, Vol. 14, No. 1, 2022, pp. 3–17. https://doi.org/https://doi.org/10.1007/s12567-021-00350-y.

[16] Linnell, J. A., and Gallimore, A. D., "Efficiency Analysis of a Hall Thruster Operating with Krypton and Xenon," *Journal of Propulsion and Power*, Vol. 22, No. 6, 2006, pp. 1402–1418. https://doi.org/10.2514/1.19613.

[17] Martinez, J. M., Rafalskyi, D., and Aanesland, A., "Development and testing of the NPT30-I2 iodine ion thruster," *36th International electric propulsion conference*, 2019.

[18] Tirila, V.-G., Hallock, A., Demairé, A., and Ryan, C. N., "Zinc Propellant Storage and Delivery System for Hall Thrusters," *AIAA Propulsion and Energy 2021 Forum*, 2021, p. 3407. https://doi.org/https://doi.org/10.2514/6.2021-3407.

[19] Marrese-Reading, C., Sengupta, A., Frisbee, R., Polk, J., Cappelli, M., Boyd, I., Keidar, M., Tverdokhlebov, S., Semenkin, S., Markusic, T., et al., "The VHITAL program to demonstrate the performance and lifetime of a bismuth-fueled very high Isp Hall thruster," *41st AIAA/ASME/SAE/ASEE Joint Propulsion Conference & Exhibit*, 2005, p. 4564. https://doi.org/10.2514/6.2005-4564.

[20] Poling, B. E., Prausnitz, J. M., O'connell, J. P., et al., *The properties of gases and liquids*, Vol. 5, Mcgraw-hill New York, 2001.

[21] Alcock, C. B., Itkin, V. P., and Horrigan, M. K., "Vapour Pressure Equations for the Metallic Elements: 298–2500K," *Canadian Metallurgical Quarterly*, Vol. 23, No. 3, 1984, pp. 309–313. https://doi.org/10.1179/cmq.1984.23.3.309.

[22] McKeon, B. J., Swanson, C. J., Zagarola, M. V., Donnelly, R. J., and Smits, A. J., "Friction factors for smooth pipe flow," *Journal of Fluid Mechanics*, Vol. 511, 2004, p. 41–44. https://doi.org/10.1017/S0022112004009796.

[23] Dworski, S., Martin, J., Ryan, C., Dyer, E., Demaire, A., and Garcia, V., "The operation of a low-power cylindrical Hall thruster with zinc as the propellant," 2019.

[24] Raitses, Y., Smirnov, A., and Fisch, N., "Cylindrical Hall Thrusters," Vol. 2, 2006. https://doi.org/10.2514/6.2006-3245.